

Critical Magnetic Neutron Scattering from Ferrous Fluoride

M. T. Hutchings*

Brookhaven National Laboratory, † Upton, New York 11973

and

M. P. Schulhof

Brookhaven National Laboratory, † Upton, New York 11973,
and State University of New York, Stony Brook, New York 11790

and

H. J. Guggenheim

Bell Telephone Laboratories, Murray Hill, New Jersey 07974

(Received 21 July 1971)

A detailed investigation of the static and dynamic correlations in the nearly ideal uniaxial anisotropic antiferromagnet FeF_2 has been carried out using quasielastic and inelastic neutron scattering. The scattering from transverse and longitudinal fluctuations can be determined separately in this compound, and the measurements test recent scaling theory and model calculations for anisotropic antiferromagnets. The transverse fluctuations are only weakly dependent on temperature, the inverse transverse correlation length $\kappa_{\perp} = (0.145 \pm 0.040) \text{ \AA}^{-1}$ at T_N , and the transverse relaxation rate $\Gamma_{\perp}(q=0, T_N) = (1.5 \pm 0.4) \text{ meV}$. The inverse longitudinal correlation length $\kappa_{\parallel}(T)$ and the staggered longitudinal susceptibility $\chi_{\parallel}(q=0, T)$ are described above T_N by the critical exponents $\nu = 0.67 \pm 0.04$ and $\gamma = 1.38 \pm 0.08$, respectively. Below T_N these remain unchanged within the experimental error. The longitudinal relaxation rates are three to five times smaller than those found in the weakly anisotropic MnF_2 . They obey a homogeneous scaling relation in (q, κ_{\parallel}) of degree close to 2, as predicted by scaling theory. The scaling function $\Omega(q/\kappa_{\parallel}) = \Gamma_{\parallel}(q, \kappa_{\parallel})/\kappa_{\parallel}^2$ bears a close resemblance to that found for MnF_2 .

I. INTRODUCTION

In the past few years the concepts of dynamic scaling¹ have been applied to the theory of second-order magnetic-phase transitions,^{2,3} and from a few assumptions definite predictions have been made for the behavior of the time-dependent correlation functions near the critical point.⁴ These correlation functions can be measured by inelastic neutron scattering,⁵ and in a series of experiments at Brookhaven and Risø the predictions of dynamic scaling theory for isotropic Heisenberg systems have been tested.⁶⁻¹³ More recently scaling theory has been extended to anisotropic systems,¹⁴⁻¹⁶ and the present investigation was carried out on an antiferromagnet with relatively large anisotropy, ferrous fluoride FeF_2 , in order to examine experimentally the applicability of scaling to such systems.¹⁷

Previous detailed experimental work on the critical scattering of neutrons from three-dimensional antiferromagnets has been confined to two compounds showing idealized properties. RbMnF_3 is a simple-cubic antiferromagnet with effectively no anisotropy, and Lau *et al.*⁷ have verified Halperin and Hohenberg's⁴ dynamic scaling predictions for temperatures above the transition for this case. A more complete investigation has been carried out on the weakly anisotropic antiferromagnet MnF_2 by Schulhof *et al.*^{9,10} MnF_2 possesses a major

advantage for neutron-scattering work as its tetragonal crystal structure leads to a unique spin direction in the sample. This enables the longitudinal and transverse correlations to be determined separately. Schulhof *et al.* were able to show that dynamic scaling provides a very good description of the longitudinal relaxation rates both above and below T_N , and they determined explicitly the scaling functions for MnF_2 .

FeF_2 has the same crystal and magnetic structure as MnF_2 but exhibits a larger anisotropy which arises from the unquenched orbital moment of the Fe^{2+} ion. The procedure adopted in the present experiment follows very closely that adopted in the investigation of MnF_2 . The scattering is, however, characterized by the anisotropy and is found to show interesting differences from the more isotropic case. The noncritical transverse spin fluctuations are suppressed by the anisotropy, and consequently we have not examined these in as much detail as the longitudinal fluctuations.

Riedel and Wegner^{14,15} predict the existence of two regimes for the critical behavior of anisotropic systems, with a crossover point characterized by a correlation length κ_{Δ}^{-1} . In one regime, close to T_N for low-fluctuation wave vectors, the anisotropic characteristics are exhibited, whereas at higher temperatures or wave vectors the isotropic behavior takes over. Our measurements on FeF_2 lie mainly in the anisotropic regime. It is

interesting to note, however, that Riedel has reinterpreted the data on the weakly anisotropic MnF_2 and shown that even in this case some of the data lie in the crossover region.¹⁸ Part of the work of Riedel and Wegner was carried out concurrently with our measurements and has been compared with our data by Riedel¹⁸; we shall refer to this comparison later.

The crystal preparation and structure, and the cryogenic details, are described in Sec. II. The theory of neutron scattering from a uniaxial antiferromagnet near the critical point is briefly reviewed in Sec. III, where the assumed forms of the cross section are given and the predictions of scaling theory summarized. In Sec. IV the quasi-elastic-scattering experiments, carried out to investigate the spatial correlations, are described. The inelastic-scattering measurements giving information on the time correlations are described in Sec. V, and a comparison of the data with scaling theory is made in Sec. VI. The conclusions are summarized in Sec. VII.

II. CRYSTAL PREPARATION, STRUCTURE, AND EXPERIMENTAL ENVIRONMENT

The sample used in the investigation was a 1.5-cm³ crystal grown by a modified Bridgman method¹⁹ at the Bell Telephone Laboratories. The starting material was synthesized by treating 99.999%-iron-metal powder in a dry hydrogen fluoride atmosphere at 900 °C. The mosaic spread of the crystal was less than 7' full width at half-maximum (FWHM); however, a small end portion of the crystal was slightly misaligned from the rest by ~15'. The crystal was mounted by clamping this portion, which was carefully shielded by cadmium so that it did not contribute to the scattering.

The crystal structure²⁰ of FeF_2 is rutile with $a = 4.697 \text{ \AA}$ and $c = 3.309 \text{ \AA}$ at room temperature. The space group is $D_{4h}^{14} - P4/mmm$, and the cation sites, surrounded by a distorted octahedron of F⁻ ions, have point symmetry D_{2h} . The magnetic structure²¹ is such that the spins align along the c axis, with the body-center ions spin antiparallel to those at the corners of the cell. The magnetic and nuclear unit cells are therefore identical.

The sample was mounted on an aluminum pedestal which was in direct thermal contact with a calibrated platinum resistance thermometer. The mount formed the bottom part of an aluminum can filled with helium gas, and the whole assembly was attached to the copper block of a Cryogenics Associates temperature-controlled Dewar, type C. T. 14. The calibration of the thermometer and the temperature measurement and control were carried out in the same manner as used for the MnF_2 experiments.^{9,11,12} Temperature control over the period of one measurement was better than

$\pm 0.001 \text{ }^\circ\text{K}$, and thermal gradients in the sample were found to be less than $\pm 0.003 \text{ }^\circ\text{K}$. The absolute temperature was estimated to be correct to $\pm 0.050 \text{ }^\circ\text{K}$, although relative temperatures were accurate to better than $\pm 0.001 \text{ }^\circ\text{K}$.

III. THEORY

A. Spin Hamiltonian for FeF_2

The spin-wave dispersion relations for FeF_2 , investigated using neutron scattering,²² show that the magnetic properties may be well described by a spin Hamiltonian of the form ($S = 2$)

$$\mathcal{H} = \sum_{\langle i,j \rangle} J_2 \vec{S}_i \cdot \vec{S}_j + \sum_i D S_i^z + \sum_j D S_j^z. \quad (1)$$

The summation in the first term is over all next-nearest-neighbor pairs (corner and body-center ions), and the single-ion terms are summed over ions on both sublattices i and j . Other interactions are found to be less than 6% of J_2 . The parameters $J_2 = 0.45 \text{ meV}$ ($5.2 \text{ }^\circ\text{K}$) and $D = 0.84 \text{ meV}$ ($9.8 \text{ }^\circ\text{K}$), so that the ratio of anisotropy field to exchange field acting on a Fe^{2+} ion is $(2S - 1)D/16J_2 = 0.35$. The single dominant intersublattice exchange interaction, and well-defined relatively high anisotropy, make FeF_2 an ideal substance in which to investigate the effects of anisotropy on critical behavior.

B. Neutron-Scattering Cross Section

1. General Form of the Cross Section

The neutron-scattering cross section for a system of N localized spins is given in general by⁵

$$\frac{\partial^2 \sigma}{\partial \Omega' \partial E'} = A(\vec{k}, \vec{k}') \sum_{\alpha\beta} (\delta^{\alpha\beta} - \hat{Q}^\alpha \hat{Q}^\beta) s^{\alpha\beta}(\vec{Q}, \omega), \quad (2)$$

where $\vec{k} = \vec{k}' - \vec{k}'$ and $\hbar\omega = E - E' = (\hbar^2/2m_0)(k^2 - k'^2)$ are the neutron momentum and energy change, respectively;

$$A(\vec{k}, \vec{k}') = \frac{N}{\hbar} \left(\frac{\gamma e^2}{mc^2} \right)^2 \frac{k'}{k} |f(\vec{Q})|^2; \quad (3)$$

γ , e , and m are the neutron gyromagnetic ratio and electron charge and mass, respectively, and $f(\vec{Q})$ is the form factor for neutron scattering.

$s^{\alpha\beta}(\vec{Q}, \omega)$ is the Van Hove scattering function²³ defined by

$$s^{\alpha\beta}(\vec{Q}, \omega) = \frac{1}{2\pi} \sum_{\vec{r}} \int_{-\infty}^{\infty} e^{i(\vec{Q} \cdot \vec{r} - \omega t)} \langle S_0^\alpha(0) S_{\vec{r}}^\beta(t) \rangle_T dt, \quad (4)$$

where $\langle \rangle_T$ denotes the thermal average. For systems such as FeF_2 with isotropic exchange and single-ion anisotropy, only the three terms $\alpha = \beta$ remain in the summation in Eq. (2).

The elastic Bragg scattering function $s_B(\vec{Q}, \omega)$ is given by the limit of the correlation function in Eq. (4) as t (or \vec{r}) $\rightarrow \infty$; the spins are uncorrelated in this limit and the cross section is proportional to

$\langle S^\alpha(\vec{Q}) \rangle^2 \delta(\omega)$. The difference $s(\vec{Q}, \omega) - s_B(\vec{Q}, \omega) = s_D(\vec{Q}, \omega)$ is the diffuse-scattering function, to which the critical fluctuations contribute. If the spatial correlations fall off according to the Ornstein-Zernike²⁴ relation, and the time fluctuations of the correlations decay exponentially, the diffuse cross section²⁵ is proportional to

$$s_D^{\alpha\alpha}(\vec{Q}, \omega) = \frac{\hbar}{\pi g^2 \mu_B^2} \frac{1}{1 - e^{-\hbar\omega\beta}} \text{Im} \chi^{\alpha\alpha}(\vec{Q}, \omega) \quad (5a)$$

$$= \frac{\hbar\omega\beta}{1 - e^{-\hbar\omega\beta}} \frac{k_B T}{g^2 \mu_B^2} \chi^{\alpha\alpha}(\vec{Q}) \frac{1}{\pi} \frac{\Gamma^{\alpha\alpha}}{\omega^2 + (\Gamma^{\alpha\alpha})^2}, \quad (5b)$$

where $\Gamma^{\alpha\alpha}$ is the relaxation rate, $\chi(\vec{Q})$ is the wave-vector-dependent susceptibility, and $\beta = 1/k_B T$. If the time fluctuations have a damped oscillatory form with frequency ω_0 and amplitude decaying exponentially, the last factor in Eq. (5a) becomes the sum of two Lorentzians with ω replaced by $\omega \pm \omega_0$. Referring the wave vector \vec{q} to an antiferromagnetic reciprocal-lattice point \vec{G} , $\vec{Q} = \vec{G} + \vec{q}$, $\chi(\vec{Q}) = A/(\kappa^2 + q^2)$ for small q . κ is the inverse correlation length ξ^{-1} , and A varies only slowly with temperature. This form of cross section has proved adequate in describing the critical scattering from a number of ferromagnets²⁶ and antiferromagnets.¹² As we shall see, we must assume the form of $s_D(\vec{Q}, \omega)$ before fitting to the data, rather than determine it directly from the data, because of the problem of deconvolution of the instrumental

resolution function.²⁷

It should be noted that Fisher²⁸ has shown that deviations from the Ornstein-Zernike Lorentzian form for $\chi(q)$ occur near T_N . At T_N he gives an expression

$$\chi(q) = [A/(\kappa^2 + q^2)]^{1-\eta/2}, \quad (6)$$

where η is a small number $\ll 1$. This form has been found to give a better fit to the data on⁸ RbMnF₃ and⁹ MnF₂ at and near T_N , with $\eta \sim 0.05 - 0.07$. We were unable to verify this for FeF₂, and shall take $\eta = 0$ in the following equations.

2. Inelastic Cross Section for FeF₂

Putting $\alpha = \beta$ in Eq. (2) and taking Oz along the c axis, the spin direction in the ordered state, we see immediately from the orientation factor $\sum_\alpha (1 - Q_\alpha^2)$ how we can separately measure the scattering from longitudinal and transverse fluctuations. If we investigate the scattering with \vec{Q} near the [001] direction, the cross section involves only $s^{xx}(\vec{Q}, \omega) = s^{yy}(\vec{Q}, \omega) = s^{\perp}(\vec{Q}, \omega)$, but if \vec{Q} is directed along [100] we measure both $s^{**}(\vec{Q}, \omega) = s^{\parallel}(\vec{Q}, \omega)$ and $s^{\perp}(\vec{Q}, \omega)$. The form factor $f(\vec{Q})$ necessitates measurements at low \vec{Q} , and the reciprocal-lattice points (001) and (100) are used for the present experiments. There is no nuclear Bragg intensity at these points, except for that from multiple Bragg scattering, and below T_N magnetic elastic scattering only occurs at (100) because of the spin direction. Near these two points we take the inelastic cross section to be

$$\frac{\partial^2 \sigma(001)}{\partial \Omega' \partial E'} = \frac{A(\vec{k}, \vec{k}')}{\pi g^2 \mu_B^2} B(\omega, T) \left[\frac{A_{(001)}}{(\kappa_{\perp}^2 + q^{*2})} \frac{1}{2} \left(\frac{\Gamma_{\perp}}{(\omega - \omega_0)^2 + \Gamma_{\perp}^2} + \frac{\Gamma_{\perp}}{(\omega + \omega_0)^2 + \Gamma_{\perp}^2} \right) \right], \quad (7)$$

$$\frac{\partial^2 \sigma(100)}{\partial \Omega' \partial E'} = \frac{A(\vec{k}, \vec{k}')}{\pi g^2 \mu_B^2} B(\omega, T) \left[\frac{A_{(100)}}{(\kappa_{\parallel}^2 + q^{*2})} \left(\frac{\Gamma_{\parallel}}{\omega^2 + \Gamma_{\parallel}^2} \right) + \frac{\lambda}{2} \frac{A_{(100)}}{(\kappa_{\perp}^2 + q^{*2})} \left(\frac{\Gamma_{\perp}}{(\omega - \omega_0)^2 + \Gamma_{\perp}^2} + \frac{\Gamma_{\perp}}{(\omega + \omega_0)^2 + \Gamma_{\perp}^2} \right) \right], \quad (8)$$

where $B(\omega, T) = \hbar\omega / (1 - e^{-\hbar\omega/k_B T})$.

The factor λ relates the relative contributions to the cross section at (100) of the transverse and longitudinal fluctuations. It is given by^{11,12}

$$\lambda = \frac{d^2 \chi_{\parallel}^{-1}(q) / d q^2}{d^2 \chi_{\perp}^{-1}(q) / d q^2} = \frac{\chi_{\perp}(Q=0)(2 + a^2 \kappa_{\parallel}^2 / 8)}{\chi_{\parallel}(Q=0)(2 + a^2 \kappa_{\parallel}^2 / 8)} \approx 1.0. \quad (9)$$

In our analysis we used values of λ varying slowly with temperature between 1.1 and 1.3 as calculated from our measured κ_{\parallel} and κ_{\perp} , and the published static-susceptibility data.²⁹ We note that if the crystal is uniformly illuminated in the beam, $\lambda A_{(100)} / A_{(001)} = 0.5$. q^* is defined by the relation

$$q^{*2} = q_a^2 + q_b^2 + (c/a)^2 q_c^2, \quad (10)$$

where a , b , c denote the crystal axes. This relation effectively expresses \vec{q}^* with respect to the cubic lattice of side a . We shall represent all reduced wave vectors, and κ , occurring in the cross sections in the units defined in Eq. (10), though for convenience the star notation will be dropped.

In writing the cross sections for critical scattering in the form given in Eqs. (7) and (8), we assume that the transverse modes are purely propagating, whereas the longitudinal modes are purely diffusive. This has been found to be the case in^{10,12} MnF₂. The frequencies ω_0 and relaxation rates Γ_{\parallel} , Γ_{\perp} will be functions of T and q , and $A_{(001)}$ and $A_{(100)}$ will vary slowly with T . Of course ω_0 may equal zero, as observed above T_N for small q , in which case the transverse component will also take on a diffusive form.

3. Quasielastic Scattering

If the quasistatic condition is satisfied, a two-axis experiment may be performed to measure the wave-vector-dependent susceptibility directly, without energy analysis. The condition states³ that the time of passage of the neutrons through a region of correlated spins should be very much less than the characteristic period of fluctuation of the spins, or that $\delta k' \ll \kappa$, where $\delta k'$ is the change in \vec{k}' due to inelasticity. When this holds, the scattering observed at a fixed scattering angle will be effectively an integration over all energy transfers ω at fixed \vec{Q} . Implicit in the condition is that $\hbar\omega \ll E_0$. If, furthermore, $\hbar\omega \ll k_B T$ at the temperature of the experiment, we see from Eqs. (6) and (7) that

$$\frac{\partial \sigma^{QE}}{\partial \Omega} (001) = \frac{A(\vec{k}, \vec{k}')}{g^2 \mu_B^2} k_B T \frac{A_{(001)}}{\kappa_1^2 + q^2} = \frac{A(\vec{k}, \vec{k}')}{g^2 \mu_B^2} k_B T \chi_1(q) \quad (11a)$$

$$= \frac{B_{(001)}^1}{\kappa_1^2 + q^2}, \quad (11b)$$

$$\frac{\partial \sigma^{QE}}{\partial \Omega} (100) = \frac{A(\vec{k}, \vec{k}')}{g^2 \mu_B^2} k_B T \left(\frac{A_{(100)}}{\kappa_{\parallel}^2 + q^2} + \frac{\lambda A_{(100)}}{\kappa_{\perp}^2 + q^2} \right) \quad (12a)$$

$$= \frac{A(\vec{k}, \vec{k}')}{g^2 \mu_B^2} k_B T \left(\chi_{\parallel}(q) + \lambda \frac{A_{(100)}}{A_{(001)}} \chi_{\perp}(q) \right) \quad (12b)$$

$$= \frac{B_{(100)}^{\parallel}}{\kappa_{\parallel}^2 + q^2} + \frac{\lambda B_{(100)}^{\perp}}{\kappa_{\perp}^2 + q^2},$$

where the B^{\perp} and B^{\parallel} are defined for convenience.

The validity of the quasistatic condition has been discussed by Lau *et al.*⁸ and Schulhof *et al.*⁹ For our experiments, using 77-meV incident neutron energy, we can infer from these papers that the condition is well satisfied in our case—particularly as Γ_{\parallel} is much smaller than for MnF_2 .

Near the transition temperature we assume that the critical longitudinal correlation lengths κ_{\parallel}^{-1} and staggered susceptibility $\chi_{\parallel}(q=0)$ diverge as

$$\begin{aligned} \kappa_{\parallel} &= \kappa_{\parallel}^+ \tau^{\nu}, & T > T_N \\ \kappa_{\parallel} &= \kappa_{\parallel}^- \tau^{\nu'}, & T < T_N \end{aligned} \quad (13)$$

and

$$\begin{aligned} \chi_{\parallel}(q=0) &= \chi_{\parallel}^+ \tau^{-\gamma}, & T > T_N \\ \chi_{\parallel}(q=0) &= \chi_{\parallel}^- \tau^{-\gamma'}, & T < T_N \end{aligned} \quad (14)$$

where $\tau = |T - T_N|/T_N$. Static scaling theory³⁰ relates γ and ν via the relation $\gamma = (2 - \eta)\nu$, and shows that $\nu = \nu'$, $\gamma = \gamma'$.

C. Dynamic Scaling Theory

In this subsection we shall briefly summarize the assumptions and predictions of scaling theory, and give the results of calculation of the form of

the scaling function by Riedel and Wegner.

The theory of dynamic scaling in isotropic magnets is based on two assumptions^{4,18}:

(i) The length and time scales of the system in the critical state are uniquely defined by the spin-spin correlation length $1/\kappa(\tau)$ and the characteristic frequency³¹ or spin relaxation time $1/\Gamma(q, \kappa)$, which both diverge at the critical point.

(ii) The two scales are related by the "scaling relation"

$$\Gamma(q, \kappa) = \tau^{\psi} \Omega(q/\tau^{\nu}) = \kappa^{\psi/\nu} \Omega(q/\kappa), \quad (15)$$

where ψ is a universal dynamic-scaling index and $\Omega(q/\kappa)$ a scale function.

Γ is thus a homogeneous function of q and κ of degree (ψ/ν) . The same expression should hold above and below T_N , but with different scaling functions Ω_+ and Ω_- which are equal at T_N . From the hydrodynamic-theory limit Halperin and Hohenberg find $\psi/\nu = \frac{3}{2}$, and as $\nu \approx \frac{2}{3}$, $\psi \approx 1$, a result which has been confirmed by recent experiments.^{7,10}

In uniaxial anisotropic systems^{4,14} the spin system is characterized by two lengths κ_{\parallel}^{-1} for the parallel critical spin components, and κ_{\perp}^{-1} for the perpendicular noncritical spin components. κ_{\parallel}^{-1} diverges as Eq. (13), whereas κ_{\perp} behaves similarly to κ_{\parallel} for high relative τ , but below a "crossover" temperature, τ_{Δ} , becomes constant at $\kappa_{\Delta}^{-1} = \kappa_{\perp}(\tau=0)^{-1}$. The longitudinal relaxation rate Γ_{\parallel} is critical, whereas Γ_{\perp} is noncritical, and the transverse fluctuations are suppressed by the anisotropy.

Riedel and Wegner¹⁵ have extended scaling theory to anisotropic substances by taking the anisotropy parameter κ_{Δ} as an additional critical variable. They start from two homogeneity assumptions for Γ , which apply either in the limit of small κ_{Δ} or for κ_{Δ} fixed. From these they recover the isotropic scaling relations if $q^2 + \kappa_{\parallel}^2 \gg \kappa_{\Delta}^2$, and a new anisotropic relation if $q^2 + \kappa_{\parallel}^2 \ll \kappa_{\Delta}^2$. In the anisotropic region they find a homogeneous function of one variable for Γ ,

$$\Gamma_n(q, \kappa_{\parallel}, \kappa_{\Delta}) = \kappa_{\Delta}^n \kappa_{\parallel}^{\psi_n/\nu_n} \Omega_n'(q/\kappa_{\Delta}^2 \kappa_{\parallel}), \quad (16)$$

where n denotes \parallel or \perp , $\xi_n = (\psi_i - \psi_n)/\nu_i$, and $p = (\nu_i - \nu_n)/\nu_i$. The indices subscripted i are those appropriate to the isotropic case, whereas those subscripted n or a are for the anisotropic case. (We shall later simply use ν for FeF_2 .) In the case of a uniaxial antiferromagnet the expression for the longitudinal fluctuations becomes

$$\Gamma_{\parallel}(q, \kappa_{\parallel}) \approx \kappa_{\parallel}^2 \kappa_{\Delta}^{3/2} W_{\parallel}(q/\kappa_{\parallel}) = \kappa_{\parallel}^2 \Omega(q/\kappa_{\parallel}), \quad (17)$$

where Ω is the new scaling function. This differs from the isotropic case in that κ_{\parallel} is raised to the power 2 rather than $\frac{3}{2}$.

At $q=0$, $\Omega(q/\kappa_{\parallel})$ equals a constant and $\Gamma(0, \kappa_{\parallel}) \propto \kappa_{\parallel}^2 \propto \tau^{2\nu}$. From the limiting form of $\Omega(q/\kappa_{\parallel})$ as $\kappa_{\parallel} \rightarrow 0$, the same power law is found to hold at T_N

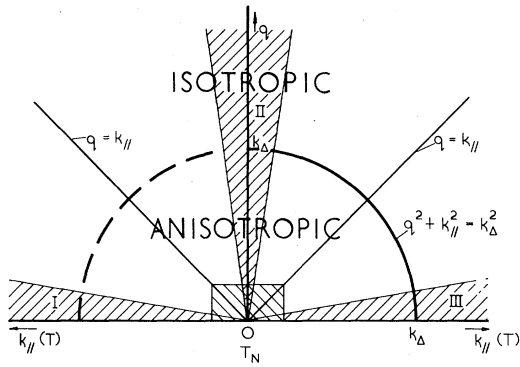


FIG. 1. Schematic plan of regions of q - $\kappa_{||}$ space. $\kappa_{||} = 0$ at T_N . Regions I and III are the macroscopic hydrodynamic regions of Ref. 4 and region II the critical region. The curve $\kappa_{||}^2 + q^2 = \kappa_{\Delta}^2$ represents the crossover between isotropic and anisotropic regimes according to Ref. 15. Regions of small q and $\kappa_{||}$ represented by the cross-hatched rectangle are inaccessible to neutron investigation because of resolution limitations.

for the q dependence of $\Gamma_{||}$.⁴ That is, $\Gamma_{||}(q, 0) \propto q^2$. These two predictions, along with the more general relation Eq. (17), are tested by our data.

The different regions of q - $\kappa_{||}$ space for an anisotropic system are shown schematically in Fig. 1. This is similar to the diagrams defining the "macroscopic hydrodynamic" regions of $q \ll \kappa_{||}$, I and III, and the "critical" region $q \gg \kappa_{||}$, II, of Halperin and Hohenberg, only there is now an additional demarcation of $q^2 + \kappa_{||}^2 = \kappa_{\Delta}^2$ between the isotropic and anisotropic regimes.

D. Theoretical Form of the Scaling Function

The form of the scaling function has up to the present time only been calculated using approximate methods. Résibois and Piette³² and Huber and Kreuger³³ have given expressions for the isotropic antiferromagnet which agree quite well with the data on RbMnF_3 . Riedel and Wegner have calculated the form of the function in the hydrodynamic region for the anisotropic case using the mode-mode approximation (MMA).^{16,18} They make specific predictions for $\Gamma_{||}$ and Γ_{\perp} for both the isotropic and anisotropic regimes. In general they find the scaling function to be independent of κ_{Δ} , as in Eq. (17). For $T > T_N$, they find that in the anisotropic regime,

$$\begin{aligned} \Gamma_{||}(\text{hydrodynamic}) &= 1.2Q\kappa_{\Delta}^{-1/2}\kappa_{||}^2, \\ \Gamma_{\perp}(\text{hydrodynamic}) &= 10Q\kappa_{\Delta}^{3/2}, \end{aligned} \quad (18)$$

whereas in the isotropic limit,

$$\Gamma_{||}(\text{hydrodynamic}) = \Gamma_{\perp}(\text{hydrodynamic}) = 4.1Q\kappa_{||}^{3/2}. \quad (19)$$

Q is proportional to the isotropic exchange coupling between the spins and is $(2.6 \pm 0.2) \text{ meV } \text{ \AA}^{3/2}$ for FeF_2 .¹⁸ We determine κ_{Δ} and $\kappa_{||}$ from experiment.

IV. QUASIELASTIC SCATTERING

A survey of the quasielastic scattering in the vicinity of the (001) and (100) reciprocal-lattice points was undertaken before the inelastic measurements were made in order to investigate the static correlations and to establish the effective temperature scale $\kappa_{||}$ and anisotropy scale κ_{Δ} .

A. Experimental Procedure

The procedure adopted was similar to that used in previous experiments.^{9,11,12} The measurements were carried out on the H4S two-axis spectrometer at the Brookhaven high flux beam reactor. Incident neutrons of one energy, 77 meV, $\lambda = 1.03 \text{ \AA}$, were used, and these were monochromated using the (311) reflection from a germanium crystal in order to minimize $\frac{1}{2}\lambda$ effects. $20'$ horizontal collimation before the monochromator was used, with $20'$ horizontal and vertical collimation before and after the sample.

The resolution function ellipsoid,²⁷ which describes the probability of detecting elastically scattered neutrons at scattering vector \vec{Q} when the instrument is set for scattering vectors \vec{Q}_0 , was determined experimentally using the (100) magnetic peak below T_N . The ellipsoid had FWHM of 0.014, 0.0023, and 0.023 \AA^{-1} in the x , y , and z directions, respectively. x is here chosen to lie along $-\vec{Q}_0$, and z is vertical. The major axis of the ellipsoid is tilted away from $0x$ by $\sim 7^\circ$, and is almost perpendicular to \vec{k}' . Use of the measured resolution at (100) will in effect allow for sample mosaic effects near (100), although these are expected to be very small. The effective values of collimation angles which gave the measured resolution function were in fact close to the nominal values. The corresponding resolution function at (001) was calculated using these effective collimation angles.

In order to take advantage of the narrowest part of the resolution function, scans were made perpendicular to the reciprocal-lattice vector, that is along \vec{c}^* through (100) and along \vec{a}^* through (001). Corrections were made for background, measured by averaging the count at a number of points near the zone boundary in different directions, and for multiple Bragg scattering. The latter was minimized by rotation of the sample about \vec{G} and was measured by scanning through the (100) and (001) positions at high temperatures, $\sim (85-95)^\circ \text{ K}$, where the critical scattering is negligible in comparison. It was not possible to correct for the magnetic Bragg intensity at (100) below T_N , and points on the scans were omitted if they contained contributions from Bragg scattering.

B. Experimental Data Analysis and Results

The transition temperature was first determined

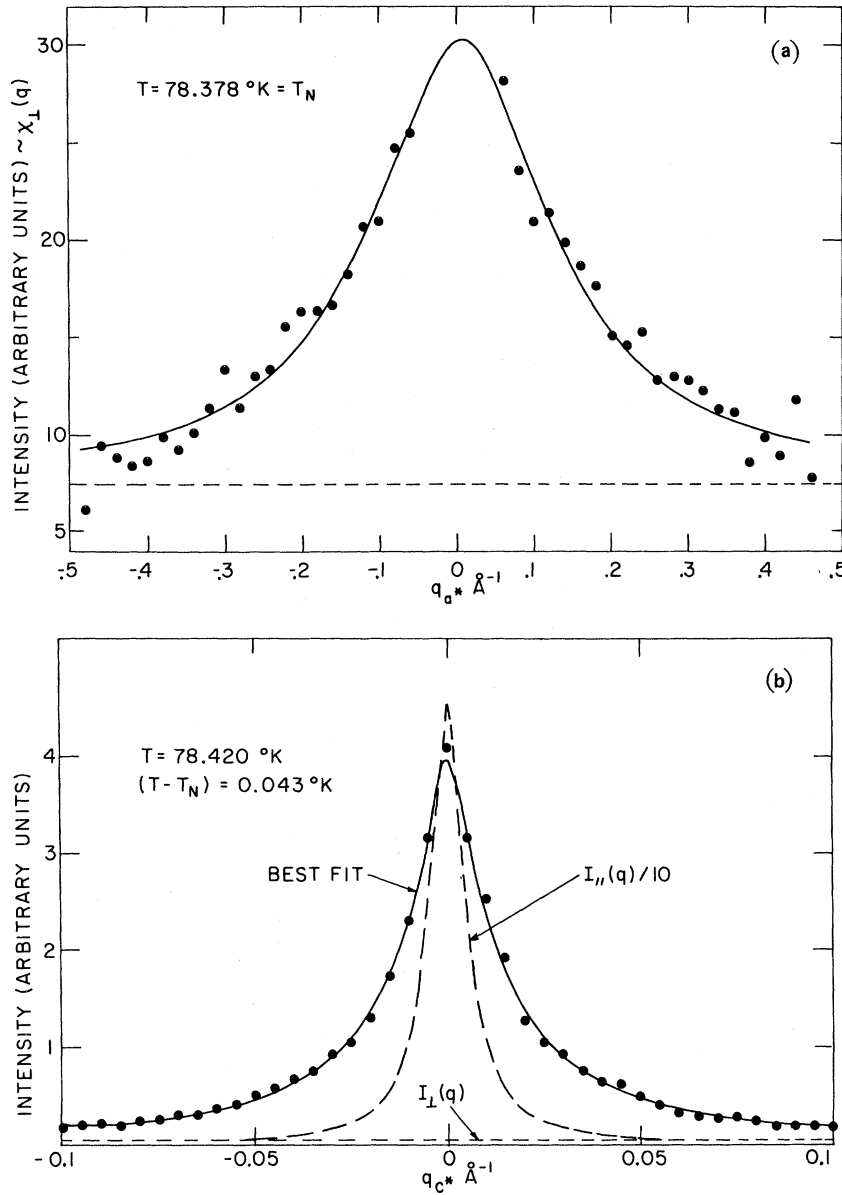


FIG. 2. (a) Quasielastic scattering from the transverse fluctuations near (001) at T_N . The points are the experimental counts and the full line the best fit of the cross section convoluted with the resolution ellipsoid. The dashed line indicates the background level. (b) Quasielastic scattering from both the transverse (weak) and longitudinal fluctuations near (100) at 78.420 °K. The solid line is the best fit of the cross section convoluted with the resolution ellipsoid to the experimental points. The dashed curves are the deconvoluted Lorentzian cross sections, not on the same scale as the experimental points. (Note that q is here in true \AA^{-1} and lies along [001].)

to 0.01 °K by monitoring the scattering near (100) as a function of temperature, and a series of scans were then made at temperature intervals ranging between 7 °K above and below T_N . It was immediately clear from scans through (100) and (001) just above T_N that the contribution from the transverse fluctuations was much weaker than that from the longitudinal fluctuations. This is a consequence of the relatively high anisotropy and corresponding large κ_{\perp} .

The theoretical expressions of Eqs. (11) or (12) were fitted to the corrected data using a least-squares fitting routine. This routine¹¹ convolutes the theoretical cross section $\sigma(\vec{Q})$ with the resolution function $R(\vec{Q} - \vec{Q}_0)$ in order to calculate the theo-

retical intensity $I(\vec{Q}_0)$:

$$I(\vec{Q}_0) = \int R(\vec{Q} - \vec{Q}_0) \sigma(\vec{Q}) d\vec{Q}. \quad (20)$$

The quality of the fits to the data was judged by the weighted variance defined by

$$\sigma_v^2 = \frac{1}{N - M} \sum_i w_i [I_i(\text{observed}) - I_i(\text{calculated})]^2, \quad (21)$$

where N is the number of data points, M the number of free parameters, and the weighting factor w_i is the inverse square of the experimental error as estimated from the counting statistics.

The transverse cross section was determined first by fitting Eq. (11b) to the data near (001).

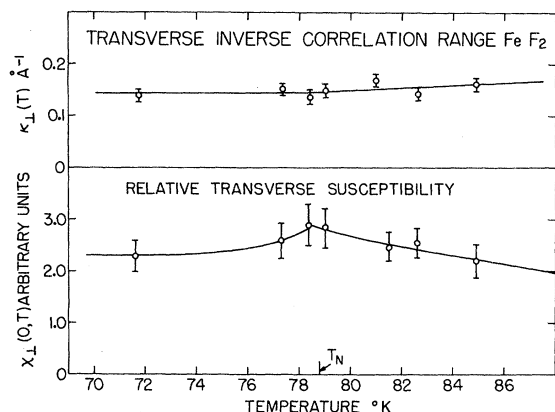


FIG. 3. Temperature variation of κ_{\perp} and $\chi_{\perp}(q=0)$ as measured from the transverse-fluctuation quasielastic scattering.

$B_{(001)}^{\perp}$, κ_{\perp} , and the effective center of the scan q_0 were treated as variable parameters. A typical scan with best fit to the data is shown in Fig. 2(a). In all cases q_0 was found to be zero within the experimental error. $\chi_{\perp}(q=0)$ was determined from the relation $\chi_{\perp}(q=0) \propto B_{(001)}^{\perp} / \kappa_{\perp}^2 T$. The results are shown in Fig. 3. It is seen that κ_{\perp} is temperature independent within the experimental error below T_N , at a value of $(0.145 \pm 0.040) \text{ \AA}^{-1}$.³⁴ This is the value of κ_{Δ} defined by Riedel and Wegner. Above T_N , κ_{\perp} rises very slightly. $\chi_{\perp}(q=0)$, the transverse staggered susceptibility, is also almost temperature independent but shows a slight rise near T_N .

The data near (100) were then fitted to Eq. (12b) treating κ_{\parallel} , $B_{(100)}^{\parallel}$, and q_0 as adjustable parameters.

λ was held fixed at the value calculated from Eq. (9) and κ_{\perp} was fixed at the value found experimentally from the (001) data. A typical scan is shown in Fig. 2(b); the line through the experimental points is the best fit of the convoluted cross section. The deconvoluted cross section is shown as the dashed lines which represent, on a different scale from the experimental points, the longitudinal and transverse contributions. We see that the transverse contribution is effectively flat and very weak at this temperature. Thus a small error in λ has a negligible effect near T_N .

Values of σ_v^2 giving the best fit to the data generally ranged between 1 and 3. A fit within statistical errors would correspond to a value of $\sigma_v^2 = 1$, and a number of trial fits were carried out to attempt to find a reason why larger values were obtained. Fits treating η [Eq. (6)] as an additional variable gave no reduction in σ_v^2 and often resulted in a negative value for η . η was therefore kept at zero for all other fits. The full expression³⁵ for the q dependence of $\chi_{\parallel}(q)$, rather than the Lorentzian small- q form, was used in some fits but gave no improvement, nor did use of a finer mesh in the integration [Eq. (20)]. We can only conclude that the somewhat large values of σ_v^2 are due to nonstatistical errors. The values of the errors on κ_{\parallel} and $B_{(100)}^{\parallel}$ do, of course, include their effects.

The temperature variation of the longitudinal inverse correlation length κ_{\parallel} above and below T_N is shown in Figs. 4 and 5, and the values of parameters in Eqs. (13) giving the best fit are summarized in Table I. T_N was determined most accurately from the fit to κ_{\parallel} , $T > T_N$, and was consequently

TABLE I. Comparison of the values of the static critical exponents in FeF_2 with those in other antiferromagnets and with theoretical estimates.

	T_N	ν	ν'	η	κ_{\parallel}^+	κ_{\parallel}^-	γ	γ'	$\chi_{\parallel}^+ / \chi_{\parallel}^-$
FeF_2 ^a	78.377 ^b ± 0.014	0.67 ± 0.04	0.7 ± 0.2	...	0.58 ± 0.07	1.36 ± 0.17	1.38 ± 0.08	1.6 ± 0.2	6.1 ± 1.0
MnF_2 ^c	67.459 ^b ± 0.014	0.634 ± 0.040	0.56 ± 0.10	0.05 ± 0.02	0.46 ± 0.02	0.57 ± 0.12	1.27 ± 0.04	1.32 ± 0.12	4.8 ± 1.0
RbMnF_3 ^d	83.019	0.724 ± 0.016	0.59 ± 0.06	0.067 ± 0.020			1.397 ± 0.068		
Ising ^e $S = \frac{1}{2}$ bcc		0.638 ± 0.002		0.041 ± 0.006			1.250 ± 0.002		5 ^f
Ising ^g (classical)		0.625 ± 0.007		~ 0.032			1.23 ± 0.02		
Heisenberg ^g (classical)		0.70 ± 0.01		~ 0.029			1.38 ± 0.02		

^aThis work.

^bAbsolute accuracy of T_N is ± 0.050 °K; the errors quoted above are those in the relative consistency of fits.

^cReference 12. (Errors correspond to 2 standard deviations.)

^dReferences 6 and 8. (Errors correspond to 2 standard deviations.)

^eReference 36.

^fReference 2.

^gReference 37.

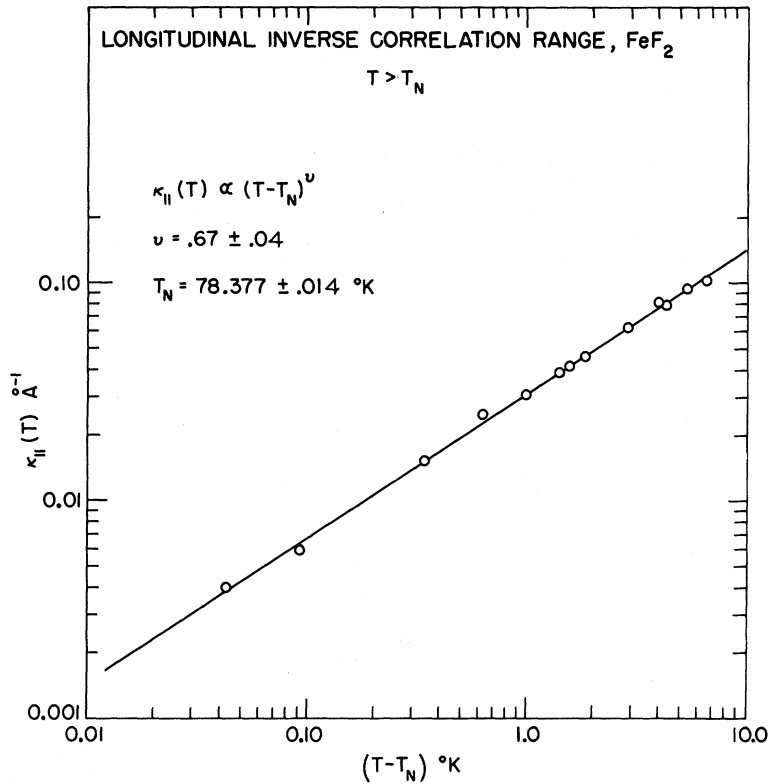


FIG. 4. Critical variation of κ_{\parallel} with temperature above T_N as determined from the quasielastic scattering. The solid line represents the best fit to the data of a power law in τ .

held fixed at this value of $78.377 \text{ } ^\circ\text{K}$ for the determination of all other temperature exponents.

The longitudinal staggered susceptibility $\chi_{\parallel}(q=0) \propto B_{(100)}^{\parallel} / \kappa_{\parallel}^2 T$ is plotted against $T > T_N$ in Fig. 6, and the exponents in Eqs. (14) found for $T > T_N$ and $T < T_N$ are given in Table I. $\chi_{\parallel}(q=0)$ may also be

determined from the inelastic-scattering measurements, and anticipating these we give a comparison of the inelastic and quasielastic data in Fig. 7. The data points have been normalized at one temperature, and the lines represent the best fits to the combined data. The parameters determined

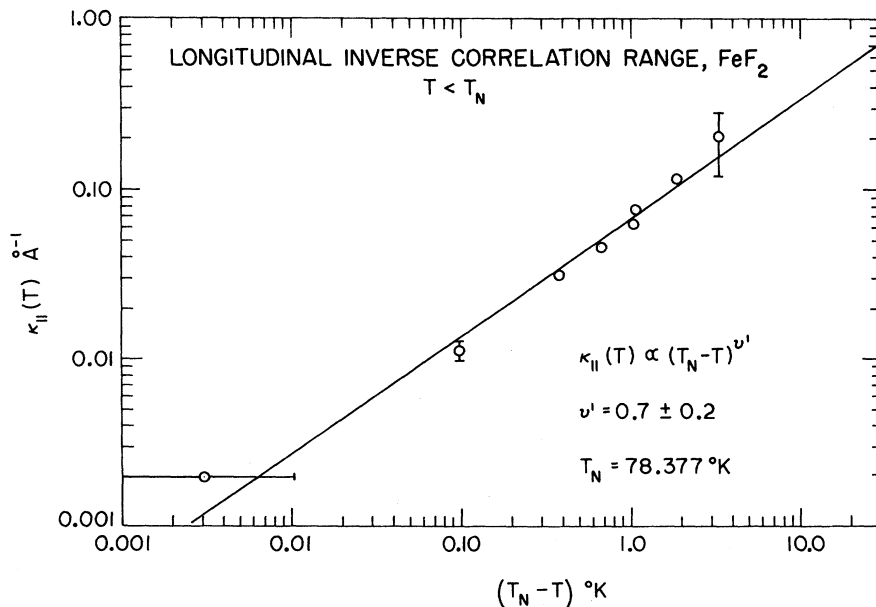


FIG. 5. Critical variation of κ_{\parallel} with temperature below T_N as determined from the quasielastic scattering. The solid line represents the best fit to the data of a power law in τ .

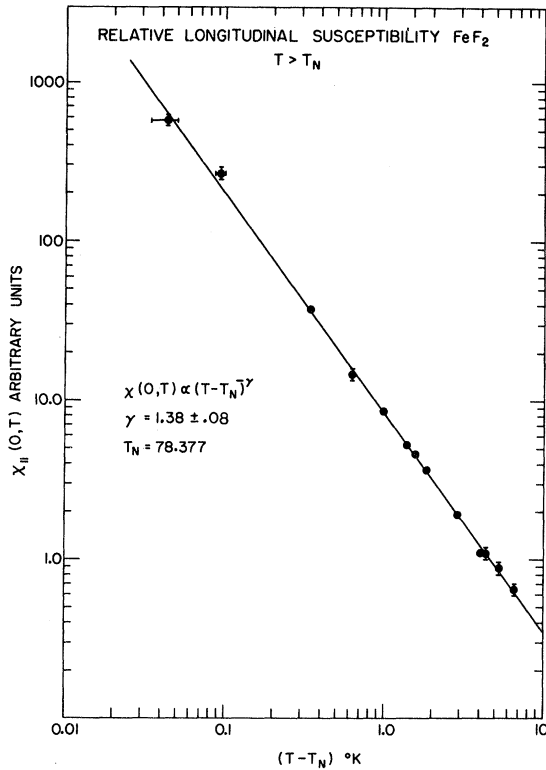


FIG. 6. Critical variation of the longitudinal staggered susceptibility above T_N as determined from the quasielastic scattering. The solid line represents the best fit to the data of a power law in τ .

from the inelastic scattering are very close (within 1/2 standard deviation) to the quasielastic values, and confirm the validity of the quasistatic approximation.

The results are compared with those for the isotropic RbMnF_3 and weakly anisotropic MnF_2 in Table I.³⁸ Calculated values are also given for two Ising cases which have been treated in detail and for the classical ($S = \infty$) case. There seems little point in commenting further on these results at this time. It is hoped that a theoretical solution for the $S = 2$ antiferromagnet with high single-ion anisotropy will become available in the near future, which may then be compared with our results.

V. INELASTIC SCATTERING

The higher anisotropy in FeF_2 causes two major differences in the inelastic critical scattering from the case of MnF_2 . The longitudinal relaxation rates are smaller by typically a fifth, and this makes their measurement more difficult, and the transverse fluctuations are noncritical and are suppressed by the anisotropy. We have concentrated our measurements on the longitudinal correlations.

A. Experimental Procedure

Measurements were carried out at three different incident energies on the H4M and H8 triple-axis spectrometers at the Brookhaven high flux beam reactor. An initial survey of the scattering was made with incident energies of 13 meV ($\lambda = 2.455 \text{ \AA}$), using the pyrolytic graphite (002) reflection for both monochromator and analyzer. 20' horizontal collimation was used in pile, before and after the sample, and before the counter. Vertical collimation was determined by the sample size and was $\sim 1.6^\circ$ FWHM. This horizontal and vertical collimation was kept constant throughout all experiments. Further measurements were made with 6-meV ($\lambda = 3.716 \text{ \AA}$) incident neutrons from a germanium (111) monochromator, using pyrolytic graphite (002) as analyzer. The very narrow linewidths near T_N necessitated special care in measurement, and these were investigated with 3.3-meV (4.965 \AA) incident neutrons obtained using the (111) reflection from a crystal of Fe_3O_4 . Pyrolytic graphite (002) was again used as analyzer, and the high content of $\frac{1}{2}\lambda$ neutrons, together with all neutrons with wavelengths less than 4 \AA , were filtered out before the counter by a beryllium filter cooled to 78°K in a Cryogenics Associates type S 017 Dewar.

The size of the resolution ellipsoid measured at

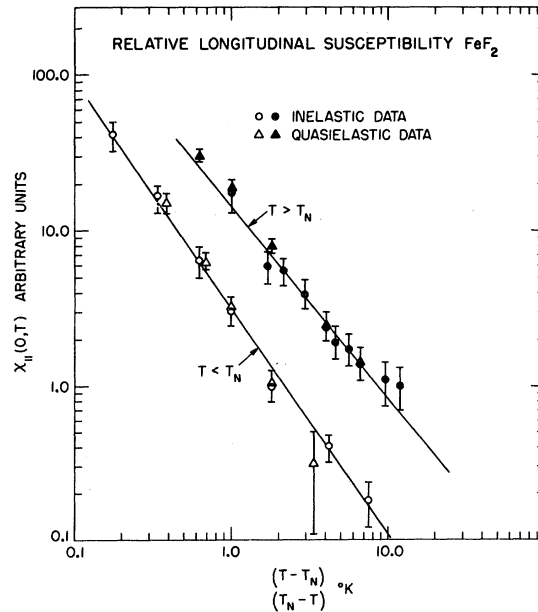


FIG. 7. Critical variation of the longitudinal staggered susceptibility above and below T_N as determined from the quasielastic and inelastic scattering. The solid lines represent the best fit of a power law in τ to both data, and yield indices given in Table I. (Note the primed exponents refer to data for $T < T_N$.)

(100) for each incident energy is summarized in Table II. The axes are those of Cooper and Nathans,³⁹ with $0x$ along $-\vec{Q}_0$ and $0z$ vertical. The "incoherent" and "Bragg" energy widths were measured using a vanadium sample and the (100) magnetic peak, respectively. The measured ellipsoids at (100) were again close to those calculated from nominal collimation angles. Effective angles corresponding to the measured resolution at (100) were used to calculate the ellipsoid at (001) for the three incident energies.

The background was determined by sampling scattering vectors near the zone boundary with the analyzer set to count neutrons with large (~ 4 meV) energy gains or losses. Counts were typically 1 per minute.

B. Experimental Data and Analysis

Measurements were made using the constant- Q technique at temperatures between 71 and 90 °K. Above T_N , \vec{Q} and \vec{q}^* were taken parallel to \vec{G}_{100} or \vec{G}_{001} . Below T_N , \vec{q}^* was taken in the [101] direction for most of the scans in order to measure the same transverse excitation at both reciprocal-lattice points.

As we have seen, the transverse scattering is much weaker than the longitudinal scattering. Furthermore, the relaxation rates are found to be larger, and consequently long counting times were necessary to investigate the scattering in detail. Measurements of the transverse scattering were, therefore, confined mainly to the temperature variation at $q=0$, and the q dependence at T_N . This was sufficient to enable the contribution at (100) to be determined.

In order to fit Eqs. (7) and (8) to the data it is necessary to assume an approximate form for the q dependence of Γ_{\parallel} , Γ_{\perp} , and ω_0 . We therefore take

$$\Gamma_{\parallel}(q, T) = \Gamma_{\parallel}(0, T) + a(T)q^2,$$

$$\Gamma_{\perp}(q, T) = \Gamma_{\perp}(0, T) + b(T)q^2,$$

and

$$\omega_0(q, T) = \omega_0(0, T) + c(T)q^2 \quad (22)$$

as a first approximation. As long as the values of the constants are chosen to describe correctly the variation over the volume of the resolution ellipsoid, their individual values need not be exactly correct.

The inelastic cross section was convoluted with the resolution ellipsoid to give the theoretical intensity $I(\vec{Q}_0, \omega_0)$,

$$I(\vec{Q}_0, \omega_0) = \int R(\vec{Q} - \vec{Q}_0, \omega - \omega_0) \sigma(\vec{Q}, \omega) d\vec{Q} d\omega. \quad (23)$$

It was then fitted⁴⁰ to the data in a systematic manner similar to that described in Refs. 11 and 12 in order to determine the parameters $A_{(001)}$, $A_{(100)}$ (which include a normalization constant), and the terms $\Gamma_{\parallel}(0, T)$, $\Gamma_{\perp}(0, T)$, $\omega_0(0, T)$, a , b , and c in Eq. (22). As few as possible of these parameters were varied at any one time. κ_{\perp} and κ_{\parallel} were held fixed at their values found from the quasielastic scattering and λ was held fixed at the appropriate calculated value. The goodness of fit σ_v^2 varied between 1.0 and 3.5.

Typical fits to the transverse data at (001) are shown in Fig. 8. The energy gap $\omega_0(0, T)$ was found to approach zero at T_N according to the relation

$$\frac{\omega_0(0, T)}{\omega_0(0, 4.2)} = \frac{\omega_0(0, T)}{6.53} = (2.7 \pm 1.0)T^{0.72 \pm 0.18} \text{ (meV)} \quad (24)$$

and remained zero above T_N . Its temperature dependence is radically different from that found in MnF_2 where the exponent is 0.37 ± 0.04 , close to that of the critical behavior of the sublattice magnetization (0.33). The exponent for the critical behavior of the sublattice magnetization in FeF_2 has been found to be 0.325 ± 0.005 .⁴¹ The transverse relaxation rate was found to vary only slowly with temperature as illustrated in Fig. 9; at T_N the rate has the value $\Gamma_{\perp}(0, T_N) = (1.5 \pm 0.4)$ meV.

The relatively weak transverse contribution was subtracted from the scattering at (100) in order to determine the longitudinal cross section. The latter takes the form of a Lorentzian with width $\sim 2\Gamma_{\parallel}$. The results for the longitudinal relaxation rates at different q and T are shown in Fig. 10. There was

TABLE II. Dimensions of the instrumental resolution ellipsoid for the inelastic-scattering measurements.

Three-axis spectrometer	E	FWHM			Incoherent (meV)	Bragg (meV)
		ΔQ_x (\AA^{-1})	ΔQ_y (\AA^{-1})	ΔQ_z (\AA^{-1})		
H4M	13 meV $\lambda = 2.45 \text{ \AA}$	0.018	0.0052	0.101	0.42	0.05
H8	6 meV $\lambda = 3.72 \text{ \AA}$	0.0078	0.0041	0.062	0.12	0.022
H8	3.3 meV $\lambda = 4.96 \text{ \AA}$	0.0074	0.0053	0.047	0.08	0.026

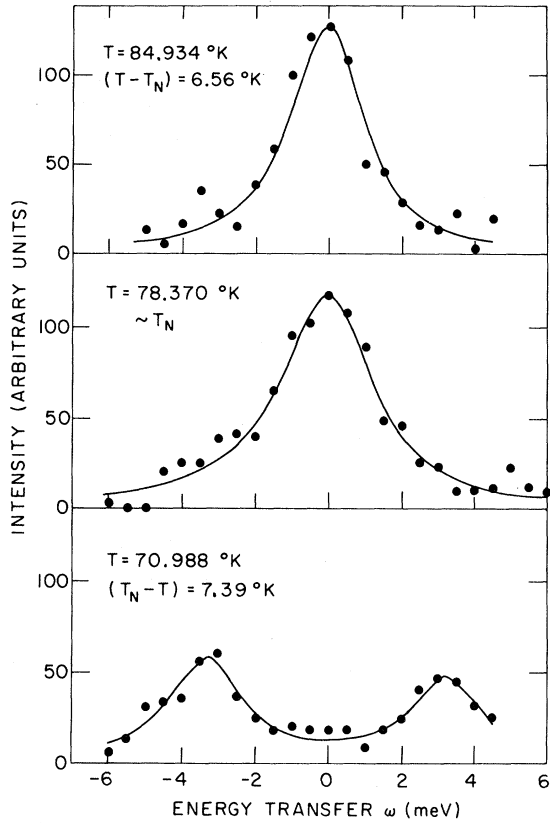


FIG. 8. Typical constant- Q energy scans of the transverse fluctuations at (001) at three temperatures, illustrating the collapse of the energy gap at T_N and its absence above T_N . The solid lines represent the best fit to the data of the cross section convoluted with the resolution function.

TABLE III. Values of parameters in Eqs. (29) giving fits to the scaling function for FeF_2 , where x is given by the relationship $x = q/\kappa$.

$\Omega(x) = A_1 + B_1x + C_1x^2 + D_1x^3$		$T > T_N$		$T < T_N$	
A_1	7.12 ± 0.6	1.28	± 0.3		
B_1	-3.96 ± 1.2	-3.27	± 0.8		
C_1	4.15 ± 0.5	2.76	± 0.4		
D_1	-0.054 ± 0.04	-0.13	± 0.02		
$\Omega(x) = A_2 + B_2x^2 + C_2x^4 + D_2x^6$		$T > T_N$		$T < T_N$	
A_2	5.92 ± 0.5	0.24	± 0.15		
B_2	2.46 ± 0.3	0.74	± 0.15		
C_2	0.014 ± 0.01	0.022	± 0.006		
D_2	-0.0003 ± 0.00002	-0.00006	± 0.00001		
$\Omega(x) = A_3 + B_3x^2$		$T > T_N$		$T < T_N$	
A_3	5.7 ± 0.5	0.75	± 0.2		
B_3	2.8 ± 0.2	-0.0015	± 0.0009		

little overlap between the data taken using different incident energies, but in cases of duplication the data with better resolution, taken with the lowest E_0 , are given. The energy widths at larger q drop sharply at T_N , whereas those at small q vary more smoothly. Below T_N there is no evidence of any speeding up of the fluctuations. These general features are very similar to those observed in MnF_2 , and Halperin and Hohenberg⁴² and Heller^{43,12} have proposed a possible explanation for the behavior below T_N .

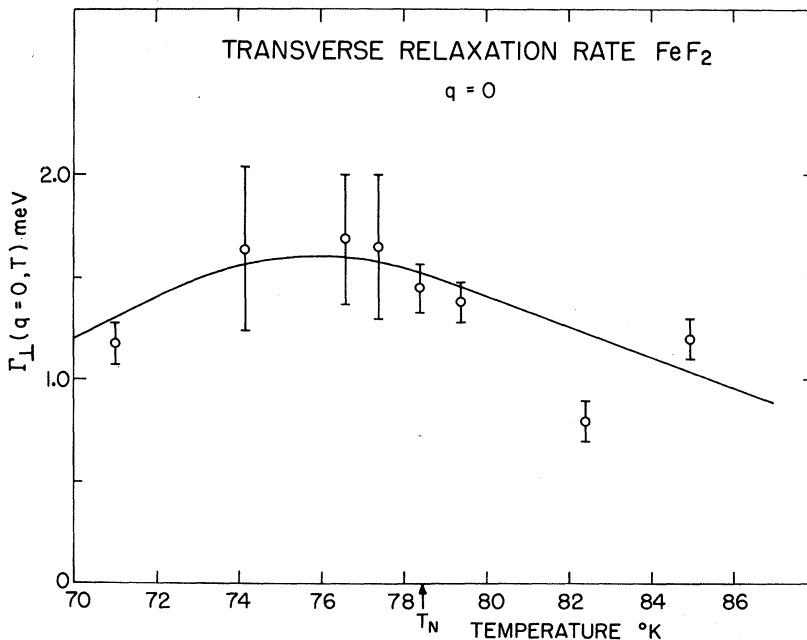


FIG. 9. Temperature variation of the transverse relaxation rate at $q=0$ as determined from the inelastic scattering.

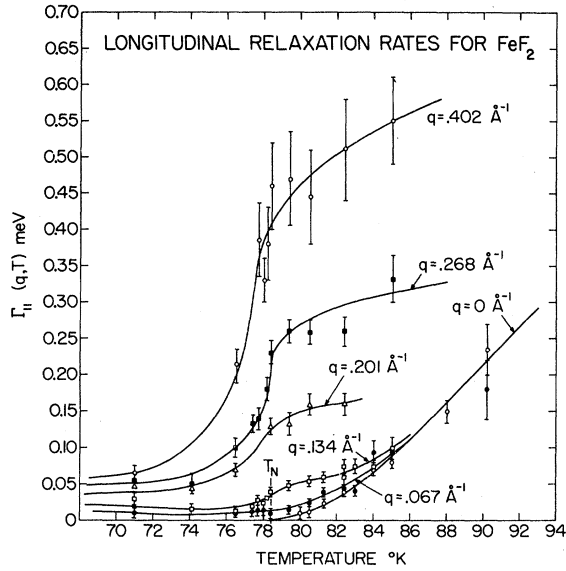


FIG. 10. Temperature and wave-vector dependence of the longitudinal relaxation rate as determined from the inelastic scattering.

VI. TEST OF DYNAMIC SCALING

In order to test the predictions of dynamic scaling in the anisotropic regime, discussed in Sec. III C, we examine the variation of the longitudinal relaxation rate in the critical and hydrodynamic regions.

In Fig. 11 the variation at T_N of $\Gamma_{||}$ with q is shown. The best fit to the data shows that the points obey the relation

$$\Gamma_{||}(q, T_N) = (3.4 \pm 1.0)q^{2.1 \pm 0.2} \text{ meV}. \quad (25)$$

The variation of $\Gamma_{||}(0, T)$ with $\kappa_{||}$ is shown in Fig. 12, where the best fit is obtained with

$$\Gamma_{||}(0, \kappa_{||}) = (17 \pm 7)\kappa_{||}^{2.3 \pm 0.4} \text{ meV}. \quad (26)$$

For the variation with temperature we obtain

$$\Gamma_{||}(0, \tau) = (4.5 \pm 1.0)\tau^{1.59 \pm 0.12} \text{ meV}. \quad (27)$$

The exponents in Eqs. (25) and (26) agree within the experimental error, as they should if scaling theory holds. They are consistent with the predicted value of 2.0 [Eq. (17)] but not with the isotropic value of 1.5. Recent nuclear-magnetic-resonance experiments also indicate an exponent of 2.0 ± 0.25 in Eq. (26) for the $\kappa_{||}$ dependence of $\Gamma_{||}(0, \kappa_{||})$, although several assumptions need to be made in the analysis of these data.⁴⁴

In Fig. 13 we plot the scaling function

$$\Omega(q/\kappa_{||}) = \Gamma(q, \kappa_{||})/\kappa_{||}^2 \quad (28)$$

determined from our measurements. It should be noted that the exponent of $\kappa_{||}$ has been chosen as 2, the theoretical value, rather than the experimental value of 2.3 giving the best fit at $q=0$. We

see that all the points do, in fact, fall very close to two general curves, one for $T > T_N$ and one for $T < T_N$. The results thus give striking evidence of the existence of a scaling function in an anisotropic antiferromagnet both below T_N , where there are no detailed theoretical predictions, as well as in the paramagnetic region. The two functions must coincide at large $q/\kappa_{||}$ in the limit $T \rightarrow T_N$. We have attempted to describe the functions $\Omega_+(q/\kappa_{||})$, $T > T_N$ and $\Omega_-(q/\kappa_{||})$, $T < T_N$ analytically by fitting to assumed functions of $(q/\kappa_{||})$. Three expressions have been tried:

$$\Omega(x) = A_1 + B_1x + C_1x^2 + D_1x^3, \quad (29a)$$

$$\Omega(x) = A_2 + B_2x^2 + C_2x^4 + D_2x^6, \quad (29b)$$

and

$$\Omega(x) = A_3 + B_3x^2, \quad (29c)$$

where $x = q/\kappa_{||}$. Each expression is found to give an adequate fit to the experimental data, and it is not possible to favor any one over the others. The values of the fitted parameters are listed in Table III.

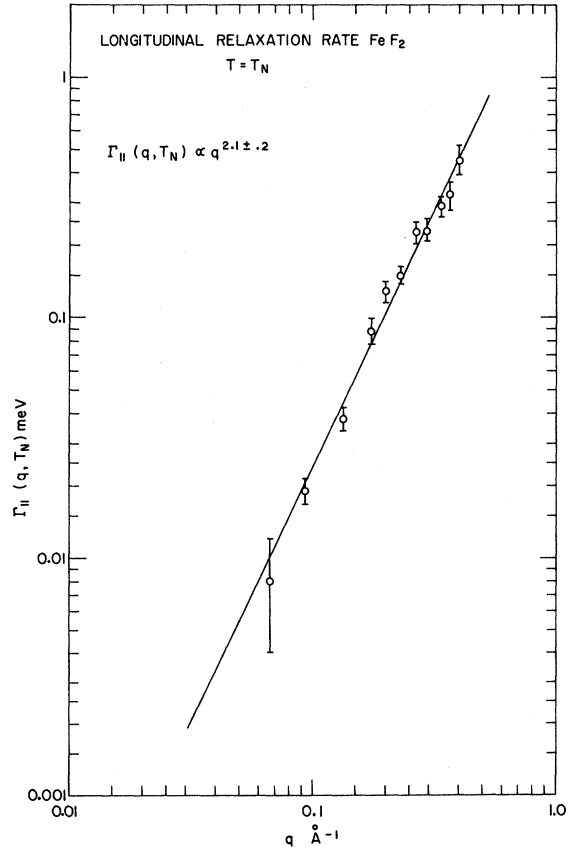


FIG. 11. Wave-vector dependence of the longitudinal relaxation rate at T_N . The solid line represents the best fit to the data of a power law in q .

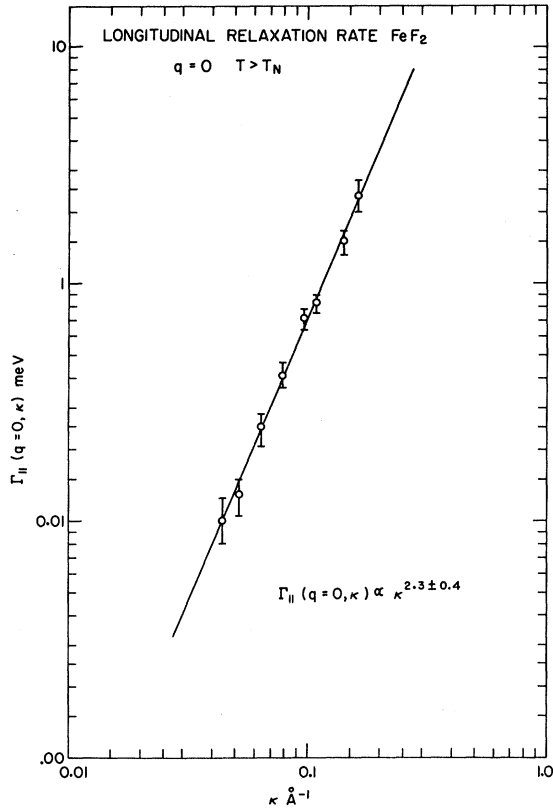


FIG. 12. Dependence of the longitudinal relaxation rate on the inverse longitudinal correlation length in the hydrodynamic region $T > T_N$. The solid line represents the best fit to the data of a power law in $\kappa_{||}$.

The functions $\Omega_{\pm}(q/\kappa_{||})$ for FeF_2 show a remarkable similarity to those found in the much more isotropic MnF_2 . This is seen in Fig. 14 where we compare the experimental points for the scaling function for FeF_2 with the smoothed experimental curves for MnF_2 and RbMnF_3 .

We may test the quantitative predictions of the MMA by a comparison of the values calculated from Eqs. (18) with Eq. (26) above and the experimental value for $\Gamma_{||}(0, T_N)$ of (1.5 ± 0.4) meV. Taking $\kappa_{\Delta} = 0.145 \text{ \AA}^{-1}$ and $Q = 2.6 \text{ meV \AA}^{3/2}$, we calculate for the hydrodynamic region

$$\Gamma_{||}(0, \kappa_{||}) = (8 \pm 2)\kappa_{||}^2 \text{ meV}$$

and

$$\Gamma_{||}(0, T_N) = (1.4 \pm 0.6) \text{ meV}.$$

The transverse relaxation rate is thus in good agreement with experiment, whereas the longitudinal rate is about a factor of 2 too small. A more complete comparison is given by Riedel.¹⁸

VII. SUMMARY AND CONCLUSIONS

Detailed measurements of the critical scattering

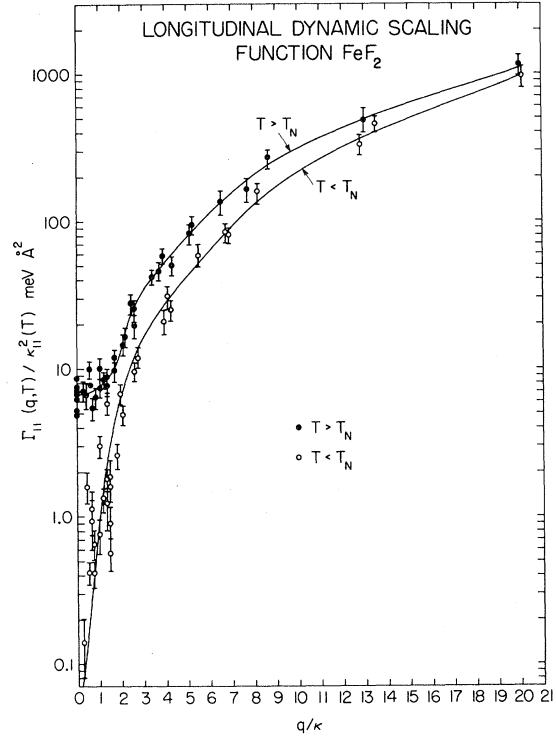


FIG. 13. Dynamic scaling functions $\Omega_{\pm}(q/\kappa_{||})$, $T > T_N$ and $\Omega_{\pm}(q/\kappa_{||})$, $T < T_N$, for longitudinal relaxation rates in FeF_2 .

of neutrons from FeF_2 have been carried out, and the nature of the static and dynamic critical phenomena in an anisotropic antiferromagnet characterized experimentally. The predictions of scaling theory for such a system have been confirmed experimentally and it has been possible to test quantitatively the form of the scaling function calculated

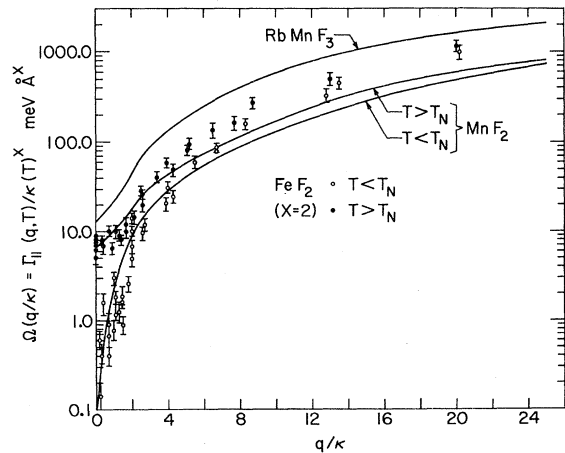


FIG. 14. Comparison of the data points for the longitudinal dynamic scaling functions $\Omega(q/\kappa_{||})$ for FeF_2 with the corresponding smoothed data curves ($X = \frac{3}{2}$) for MnF_2 and RbMnF_3 (Refs. 7, 10, 12).

for the hydrodynamic region in the MMA by Riedel and Wegner.

The transverse fluctuations are noncritical and give relatively weak scattering which, in contrast to the more isotropic case MnF_2 , is not strongly temperature dependent. The characteristic length $\kappa_{\perp}(T_N)^{-1} = \kappa_{\Delta}^{-1}$, which sets the scale of the anisotropy is determined to be $0.145^{-1} = 6.9 \text{ \AA}$, and many of our measurements are carried out within the anisotropic regime of scaling theory, $q^2 + \kappa_{\parallel}^2 \ll \kappa_{\Delta}^2$. The transverse relaxation rate at zero wave vector is in good agreement with that calculated in the MMA.

The longitudinal relaxation rates show the same general variation with temperature and wave vector as found for MnF_2 . They are, however, of the order of a fifth smaller, and are described by a homogeneous scaling function of q and κ_{\parallel} of degree 2

rather than of degree $\frac{3}{2}$ as found in the isotropic systems. This is in agreement with recent anisotropic scaling theory. The scaling functions $\Omega_{\pm}(q/\kappa_{\parallel})$ are remarkably close to those found in MnF_2 . In the hydrodynamic region the rates are a factor of 2 larger than predicted by the MMA calculations.

Together with previous investigations on the isotropic RbMnF_3 and weakly anisotropic MnF_2 the present results help to clarify the general experimental features of the critical behavior of three-dimensional antiferromagnetic systems.

ACKNOWLEDGMENTS

We are extremely grateful to P. Heller, R. Nathans, and E. K. Riedel for many helpful discussions. We also acknowledge the interest and advice of M. Blume and G. Shirane.

†Work performed under the auspices of the U. S. Atomic Energy Commission.

*Present address: Atomic Energy Research Establishment, Harwell, Didcot, Berks, England.

¹R. A. Ferrell, N. Menyhard, H. Schmidt, F. Schwabl, and P. Szeffalussy, *Phys. Rev. Letters* **18**, 891 (1967).

²M. E. Fisher, *Rept. Progr. Phys.* **30**, 615 (1967).

³P. Heller, *Rept. Progr. Phys.* **30**, 731 (1967).

⁴B. I. Halperin and P. C. Hohenberg, *Phys. Rev. Letters* **19**, 700 (1967); *Phys. Rev.* **177**, 952 (1969).

⁵W. Marshall and R. D. Lowde, *Rept. Progr. Phys.* **31**, 705 (1968).

⁶L. M. Corliss, A. Delapalme, J. M. Hastings, H. Y. Lau, and R. Nathans, *J. Appl. Phys.* **40**, 1278 (1969).

⁷H. Y. Lau, L. M. Corliss, A. Delapalme, J. M. Hastings, R. Nathans, and A. Tucciarone, *Phys. Rev. Letters* **23**, 1225 (1969).

⁸H. Y. Lau, L. M. Corliss, A. Delapalme, J. M. Hastings, R. Nathans, and A. Tucciarone, *J. Appl. Phys.* **41**, 1384 (1970).

⁹M. P. Schulhof, P. Heller, R. Nathans, and A. Linz, *Phys. Rev. B* **1**, 2304 (1970).

¹⁰M. P. Schulhof, P. Heller, R. Nathans, and A. Linz, *Phys. Rev. Letters* **24**, 1184 (1970).

¹¹M. P. Schulhof, BNL Report No. 14712, 1970 (unpublished).

¹²M. P. Schulhof, R. Nathans, P. Heller, and A. Linz, *Phys. Rev. B* **4**, 2254 (1971).

¹³O. W. Dietrich, *J. Phys. C* **2**, 2022 (1969).

¹⁴E. Riedel and F. Wegner, *Z. Physik* **225**, 195 (1969).

¹⁵E. Riedel and F. Wegner, *Phys. Rev. Letters* **24**, 730 (1970).

¹⁶E. Riedel and F. Wegner, *Phys. Letters* **32A**, 273 (1970).

¹⁷A short account of this work was presented at the 16th Annual Conference on Magnetism and Magnetic Materials, Miami Beach; see M. P. Schulhof, M. T. Hutchings and H. J. Guggenheim, *J. Appl. Phys.* **42**, 1376 (1971).

¹⁸E. Riedel, *J. Appl. Phys.* **42**, 1383 (1971).

¹⁹H. J. Guggenheim, *J. Appl. Phys.* **34**, 2482 (1963).

²⁰J. W. Stout and S. A. Reed, *J. Am. Chem. Soc.* **76**, 5279 (1954).

²¹R. A. Erickson, *Phys. Rev.* **90**, 779 (1953).

²²M. T. Hutchings, B. D. Rainford, and H. J. Guggenheim, *J. Phys. C* **3**, 307 (1969).

²³L. Van Hove, *Phys. Rev.* **95**, 249 (1954); **95**, 1374 (1954).

²⁴L. F. Ornstein and F. Zernike, *Proc. Acad. Sci. Amsterdam* **17**, 793 (1914); *Z. Physik* **19**, 134 (1918); **27**, 761 (1926).

²⁵We shall adopt the notation of Marshall and Lowde (Ref. 5) wherever possible. This differs somewhat from that of some other authors, notably that of Halperin and Hohenberg (Ref. 4), and Lau *et al.* (Ref. 7) who use symmetrized correlation functions. Halperin and Hohenberg furthermore consider the correlation function, rather than the staggered susceptibility, to diverge as an exponential power of $\tau = (T - T_N)/T_N$.

²⁶See, for example, M. F. Collins, V. J. Minkiewicz, R. Nathans, L. Passell, and G. Shirane, *Phys. Rev.* **179**, 417 (1969); V. J. Minkiewicz, M. F. Collins, R. Nathans, and G. Shirane, *ibid.* **182**, 624 (1969); J. Als-Nielsen, *Phys. Rev. Letters* **25**, 730 (1970).

²⁷M. J. Cooper and R. Nathans, *Acta Cryst.* **A24**, 481 (1968); **A24**, 619 (1968).

²⁸M. E. Fisher, *J. Math. Phys.* **5**, 944 (1964).

²⁹S. Foner, *Proceedings of the International Conference on Magnetism, Nottingham*, 1964 (Institute of Physics and the Physical Society, London, 1964), p. 438.

³⁰L. P. Kadanoff, W. Götze, D. Hamblen, R. Hecht, J. Kane, E. A. S. Lewis, V. V. Palciauskas, M. Rayl, and J. Swift, *Rev. Mod. Phys.* **39**, 395 (1967).

³¹The characteristic frequency of Ref. 4 is defined from the integral over all the frequency distribution, and is more general than the rates $\Gamma(q, \kappa)$ which it equals for the longitudinal fluctuations, or transverse fluctuations at $\omega_0 = 0$. We are mainly concerned with $\Gamma_{\parallel}(q, \kappa)$ in this paper.

³²P. Résibois and C. Piette, *Phys. Rev. Letters* **24**, 514 (1970).

³³D. L. Huber and D. A. Krueger, *Phys. Rev. Letters* **24**, 111 (1970).

³⁴We shall quote all errors in measured numbers as two standard deviations (sd), corresponding to a 95% confidence limit. The error bars on plotted experimental points, however, correspond to 1 sd.

³⁵See, for example, T. Moriya, *Progr. Theoret. Phys.* (Kyoto) **28**, 371 (1962).

³⁶M. A. Moore, D. Jasnow, and M. Wortis, *Phys. Rev. Letters* **22**, 940 (1969).

³⁷D. Jasnow and M. Wortis, *Phys. Rev.* **176**, 739 (1968).

³⁸A value of $\gamma = 1.33 \pm 0.10$ has been found for KMnF_3 ; see M. J. Cooper and R. Nathans, *J. Appl. Phys.* **37**, 1041 (1966).

³⁹M. J. Cooper and R. Nathans, *Acta Cryst.* **23**, 357

(1967).

⁴⁰The program used was a modified form of that written by Lau *et al.*, Ref. 7, and is described in Ref. 11.

⁴¹G. K. Wertheim, *J. Appl. Phys.* **38**, 971 (1967).

⁴²B. I. Halperin and P. C. Hohenberg, *Phys. Rev.* **188**, 898 (1969); see also P. C. Hohenberg (unpublished).

⁴³P. Heller, *Intern. J. Magnetism* **1**, 53 (1970).

⁴⁴A. Gottlieb and P. Heller, *Phys. Rev. B* **3**, 3615 (1971).

PHYSICAL REVIEW B

VOLUME 5, NUMBER 1

1 JANUARY 1972

Nature of Coupled Modes in a Ferromagnetic Insulator*

B. A. Huberman† and E. Burstein

*Department of Physics and Laboratory for Research on the Structure of Matter,
University of Pennsylvania, Philadelphia, Pennsylvania 19104*

and

R. Ito

Hitachi Central Research Laboratories, Kokubungi, Tokyo, Japan

(Received 6 July 1971)

The dispersion relation for the coupled photon-magnon-phonon modes is discussed, and an expression for the time-averaged energy density of the coupled modes in a ferromagnetic insulator is derived, based on the electromagnetic nature of the modes. The phenomena of ferromagnetic resonance and ferroacoustic resonance are shown to correspond to specific frequency-wave-vector regimes of the dispersion curves. Expressions are derived for the phonon, magnon, and photon strengths of the coupled modes in the two regimes.

I. INTRODUCTION

In a ferromagnetic insulator, the electromagnetic and acoustic eigenmodes of the crystal are coupled acoustic phonon-magnon-“photon” modes,¹ which arise from the magnetoelastic interaction of acoustic phonons with magnons² and the magnetic dipole interaction of photons and magnons.³ In the present paper we are not directly concerned with the coupling of the photons with optical phonons nor with other electric dipole excitations,⁴ and therefore designate the coupled photon-electric dipole-excitation (polariton) modes simply as “photons.”

The existence of the coupled acoustic phonon-magnon-photon modes implies that whenever an electromagnetic wave or an acoustic wave is incident on a ferromagnetic crystal, the propagating modes will be an admixture of acoustic phonons, magnons, and photons, whose relative amplitudes depend on the wave vector and frequency of the incident wave. Since the properties of the coupled modes, i. e., the damping of the modes and the nonlinear interactions of the modes with other excitations, depend on the acoustic phonon, magnon, and photon contents of the modes, it is desirable to have expressions for the phonon, magnon, and photon strengths of the coupled modes as a function

of frequency and wave vector.

In Sec. II, the dispersion relation of the coupled photon-magnon-phonon modes is discussed, and an expression for the time-averaged energy density of the coupled modes in the crystal is obtained, based on the equivalence of the coupled modes and the electromagnetic modes in the crystal.

In Sec. III, a general expression is obtained for the acoustic phonon, magnon, and photon strengths of the modes. Simple analytical equations are obtained for two different frequency-wave-vector regimes: (a) the ferromagnetic resonance regime and (b) the ferroacoustic resonance regime.

In Sec. IV, the damping of the coupled modes is discussed, as one example of the usefulness of the expressions for the phonon strength, magnon strength, and photon strength.

II. DISPERSION RELATION AND ENERGY DENSITY

For a cubic crystal, the Hamiltonian density is given by⁵

$$H = (1/2\rho)(\pi_x^2 + \pi_y^2 + \pi_z^2) + \frac{1}{2}\alpha(\Sigma_{xx}^2 + \Sigma_{yy}^2) \\ + b(M_x \Sigma_{yx} + M_y \Sigma_{xx}) + (H^2 + \vec{E} \cdot \vec{D})/8\pi + \frac{1}{2}(\omega_0/\omega_s) \\ \times (M_x^2 + M_y^2) - \vec{M} \cdot \vec{H} \quad , \quad (1)$$